Metallic Cation-Mediated Entrapment of Nucleic Acids on Mesoporous Silica Surface: Application in Castration Resistant Prostate Cancer

Angelea Maestas-Olguin[1*], Marian Olewine[1], Sheymah Thabata[2], Johanna Tsala Ebode[1], Mariella Arcos[3], Jacob Krawchuck[4], Eric N. Coker[5], Adrian J. Brearley[6], Xiang Xue[3], John Watt[7], Achraf Noureddine[1*], C. Jeffrey Brinker[1*]

[1]Department of Chemical and Biological Engineering, University of New Mexico, Albuquerque, NM, United States, 87131

[2]Department of Biochemistry School of Medicine, University of New Mexico, Albuquerque, NM, United States, 87131

[3]Department of Biochemistry and Molecular Biology, University of New Mexico, Albuquerque, NM, United States, 87131

[4]Center for Integrated Nanotechnologies, Sandia National Laboratories, Albuquerque, NM, United States, 87123

[5]Department of Applied Optical/Plasma Sciences, Sandia National Laboratories, Albuquerque, NM, United States, 87123

[6]Department of Earth and Planetary Sciences, University of New Mexico, Albuquerque, NM, United States, 87131

[7] Center for Integrated Nanotechnologies, Los Alamos National Laboratory, Los Alamos, NM, United States, 87545

*Email: angemaestas13@unm.edu, anoureddine@unm.edu, jbrinker@unm.edu

Abstract

The use of exogenous nucleic acid technologies to modulate aberrant protein expression resulting from genetic mutations is a promising therapeutic approach for treatment of diseases such as advanced prostate cancer (PC). The promise of nucleic-based therapeutics is dependent on the development of platforms that effectively protect nucleic acids from nuclease degradation and deliver the nucleic acids to the cytosol of target cells. In this work, we present the development of a divalent metal-mediated nucleic acid entrapment strategy withing porous silica matrix. This simple strategy results in efficient loading percentages of both siRNA (>60%) and mRNA (>80%) as well their release within relevant biological environments (80%). Additionally, our data supports that the current method reduces endosomal entrapment. and supports the lipid coating of mesoporous silica nanoparticles (LC-MSNs). The metal-enhanced nanosystem is assessed for biocompatibility, stability, and circulation within *in vitro, ex ovo* and *in vivo* models of PC.

1. Intro/Background

Treatment of advanced prostate cancer (PC) has moved to FDA approved androgen signaling inhibitors (enzalutamide and abiraterone) with some increase in overall survival. Unfortunately, advanced PC diseases become castration resistant after relapse and metastasis to sites such as bone, liver, lymph nodes and brain are observed.[1] To reduce the burden of these diseases and improve patient outcomes, it is vital to develop new therapeutic approaches that address hard to treat cancers such as advanced prostate cancer. The limitations and issues associated with traditional prostate cancer therapeutics as well as enhanced understanding of the molecular mechanisms leading to disease progression have driven the emergence of nucleic acid-based gene therapies.[2–7] More specifically, the utilization of synthetic siRNAs or mRNAs for modulation of gene expression are attractive for use in therapeutics due to their high specificity and the ability to tailor their design for a broad range of genetic targets.[8,9]

In the last ten years, numerous scientific studies have been reported in the literature focused on gene therapy for cancers, however very few gene therapies have achieved FDA approval for use in clinical settings. The reason for this is related to issues associated with the delivery of naked DNA/RNA molecules in biological systems such as degradation by nucleases, rapid clearance by the kidneys, poor cellular uptake and non-specific biodistribution.[10] These physiological barriers for nucleic acid delivery necessitate the development of carriers that provide safe and efficient delivery of nucleic acids to target tissues. The application of nanotechnology for nucleic acid delivery has enabled the development of nonviral systems that provide effective gene modulation. Material properties of nanoparticle systems must enable stable blood circulation after intravenous injection, evasion of the mononuclear phagocytic and reticuloendothelial systems, facilitate uptake by target cells and subsequent endosomal escape for cytosol delivery upon cellular internalization. Lipid-based nanocarriers systems (namely liposomes and solid lipid nanoparticles) have emerged as promising delivery agents for nucleic acids due to their biocompatibility, ability to protect naked DNA/RNA from degradation and clinical translatability.[11–14] While promising, liposomal based nanoparticles have some limitations in their stability, loading capacity and multi-cargo accommodation and reliance on specific lipid components for effective nucleic acid encapsulation.[15,16] Mesoporous silica nanoparticles (MSNs) resulting from surfactant templated sol gel processes have garnered significant attention within biomedical research due to their colloidally stability, controllable size and morphology, chemical versatility, excellent biocompatibility and tunability to a variety of nucleic acid cargos.[17–20] Additionally, MSNs have been shown to improve liposome stability, enhance blood circulation and stability as well as offer controlled release characteristics.[17,21,22] Native bare silica matrix exhibit a net negative charge in aqueous environments due to the presence of silanolate groups at their surface which presents an unfavorable electrostatic repulsive interaction between silica mesopores and negative charged nucleic acid molecules. To overcome these interactions, various so called “core-shell” constructs have been developed in which silica surface modifications[23,24] and cationic polymers[25–29] or cationic lipid coatings[13,30] are employed. While these cationic modifications of the silica surface have had success in loading of nucleic acids, they face shortcomings in 1) the blood circulation as positively charged molecules tend to stick to negatively charged membrane of vasculature epithelial cells 2) the ability to release cargos in biological conditions and 3) issues with cationic mediated toxicity.

In this study, we present the development of a new nucleic acid entrapment strategy that reduces the need of positively charged organic moieties, polymers, or complicated silica surface functionalization steps to a single metallic cation that efficiently intermediates the interaction between the silica surface and nucleotide’s phosphate locking-in the nucleic acid. This method results in efficient loading via a straightforward incubation, but also quick release within biologically relevant environments. This simple strategy also allows and supports the addition of a lipid coating on the silica surface hence combining physiologically relevant liposomes with colloidally stable silica nanoparticles for delivery of nucleic acids in the advanced PC landscape. The addition of this metal cation entrapment technique also serves to provide a mechanism of endosomal escape for cytosolic delivery of siRNA or mRNA. Finally, the LC-MSN’s nucleic acid delivery ability, circulation and biocompatibility were evaluated within relevant *in vitro, ex ovo* and *in vivo* models of PC.

2. Experimental Section

Chemicals. Tetraethylorthosilicate (TEOS), cetyltrimethylammonium chloride (CTAC), cetyltrimethyl ammonium bromide (CTAB), triethanolamine (TEA), calcium chloride ($CaCl_2$), sodium chloride (NaCl), magnesium sulfate ($MgSO_4$), iron III chloride ($FeCl_3$), aluminum III chloride ($AlCl_3$), ammonium nitrate (NH_4NO_3), hydrochloric acid (HCl), cyclohexane, (3-Aminopropyl)triethoxysilane (APTES) and dimethylformamide (DMF) were purchased from Sigma Aldrich. Cyanine 3-NHS (Cy3) was purchased from Luminoprobe and DyLight 633-NHS was purchased from ThermoFisher. Potassium chloride (KCl) and ammonium hydroxide (NH_4OH) were purchased from Macron Chemicals. Anhydrous ethanol was purchased from Thomas Scientific. Magnesium chloride ($MgCl_2$) was purchased from Mallinckrodt Chemicals. 1,2-dipalmitoyl-sn-glycero-3-phosphocholine (DPPC), cholesterol, 1,2-distearoyl-sn–glycero-3-phosphoethanolamine-N-[methoxy–(polyethylene glycol)−2000] (ammonium salt) (DSPE-PEG_{2000}), 1,2-dioleoyl-3-trimethylammonium-propane (chloride salt) (DOTAP), 1,2-dioleoyl-sn–glycero-3-phosphoethanolamine (DOPE), 1,2-distearoyl-sn-glycero-3-phosphoethanolamine-N-[carboxy(polyethylene glycol)-2000, NHS ester] (sodium salt) (DSPE-PEG_{2000}-NHS) were purchased from Avanti Polar Lipids.

Synthesis of monodisperse 2nm pore size hexagonal silica nanoparticles. In a 150 mL beaker, 0.29g of CTAB was combined with 150g of a 0.32M NH_4OH in water solution. The beaker was then covered with parafilm before being placed in an oil bath at 40 °C. The reaction mixture was stirred at 600 rpm for one hour. The parafilm was then removed and a solution of 0.6 mL TEOS in 2.4 mL ethanol was added to the beaker and reacted for 30 minutes before stirring was stopped. The reaction was allowed to age at 40 °C overnight before being placed in an oven at 70 °C for a 24-hour hydrothermal treatment. Finally, the resulting suspension of MSNs was centrifuged at 50,000 g. Surfactant removal was achieved via successive washing steps with NH_4NO_3 (6 g/L) and HCl (1% in ethanol, twice). All centrifugation steps were conducted at 50,000 g for 15 minutes. Finally, the resulting MSNs were stored in pure ethanol.

Synthesis of monodisperse 8 and 5nm pore size spherical silica nanoparticles. In a 100 mL round bottom flask, 0.181g of TEA, 24 mL of CTAC and 36 mL of DI H_2O were mixed in an oil bath at 55°C for one hour with a stirring speed of 400 rpm. The stirring speed was then reduced to 200 rpm before adding dropwise a solution of TEOS in cyclohexane (2 mL TEOS, 18 mL cyclohexane). The mixture was then allowed to react for 18 hours before being removed from heat and stirring. The upper organic phase was removed from the flask and the resulting aqueous phase was centrifuged at 50,000 g. Surfactant removal was conducted in the same manner as described for hexagonal MSNs. The resulting MSNs are stored in pure ethanol.

For *in vitro* and *in vivo* studies, MSNs were dyed with either Cy3 or Dylight 633. For Cy3 labeled MSNs, a solution of Cy3 and APTES in ethanol (2 mg Cy3, 2 μL APTES, 1 mL ethanol) was added to the aqueous phase 10 minutes before TEOS addition. For Dylight 633 labeled MSNs, APTES (110 μL APTES in 200 μL ethanol) was added to the aqueous phase during the MSN synthesis (18 hours after TEOS addition) and allowed to react for three hours before surfactant removal. The resulting amine functionalized MSNs were readily reacted with AF 633 NHS for 2 hours. The MSN suspension was spun down and the supernatant was replaced by a solution of succinic anhydride (100 mg in 4 mL DMF) and the mixture was sonicated for 2 min and kept at RT for at least 24 h. The labeled MSNs were then spun down and washed once by DMF and twice by ethanol.

Nanoparticle Characterization. TEM/STEM and SEM images were obtained on a JEOL NEOARM 200 kV aberration corrected instrument equipped with a Gatan Orius digital camera system. Energy dispersive spectroscopy (EDS) mapping was also conducted on the JEOL NEOARM STEM instrument equipped with JEOL SDD 100 mm^2 EDS detectors. MSN hydrodynamic size, zeta potential and polydispersity were assessed using dynamic light scattering (DLS) on a Malvern Zetasizer Nano-ZS equipped with a He–Ne laser (633 nm) and non-invasive backscatter optics. All samples for DLS measurements were suspended in distilled water or ethanol at a 1 mg mL −1 concentration. Samples were washed three times through centrifugation prior to measurements. All measurements were acquired at 25 °C. DLS measurements for each sample were obtained in triplicate and the Z-average diameter was used for all reported hydrodynamic size values. The zeta potential for all the samples was measured in distilled water in triplicate according to the Smoluchowski method. All reported values correspond to the average of three independent measurements. Nitrogen adsorption–desorption isotherms of MSNs were obtained on a Micromeritics ASAP 2020 at 77 K. Samples were degassed at 60 °C for 12 h before measurements. The surface area was calculated following the Brunauer–Emmet–Teller (BET) equation and the pore size was obtained using the standard Barrett–Joyner–Halenda (BJH) method applied to both the adsorption and desorption branches. For visualization of LC-CaMSNs, samples (1 mg/mL in 1x PBS) were plunge frozen into liquid ethane using a Thermo Fisher Scientific Vitrobot, then Cryo-TEM imaging was performed on a Talos L120C operating at 120 kV using a Gatan 626 holder.

Metal Based Cation siRNA Loading. The metal-based cation loading procedure described here was adapted and developed from a previously described method for porous silicon.[31] Stock solutions of cation solutions were prepared by adding corresponding mass of cation salt to 10 mL of DI H2O to achieve final concentrations of 0.4M, 1M or 4M and used immediately for loading experiments. 1 mg of MSNs were washed twice in DI H_2O (1 mg/100 µL) before being incubated with a 5% weight ratio of Cy3 siRNA (ThermoFisher AM4621) or Cy5 firefly luciferase mRNA (APExBio R1010) for 10 minutes. 750 µL of the cation solution was then added to the MSN-nucleic acid suspension and allowed to incubate at room temperature for 1 hour. The resulting nucleic acid loaded MSNs were then spun down at 20,000 g and washed twice with DI H_2O (Sigma Aldrich W4502 pH=8.8). Loading efficiencies were quantified using a Biotek microplate reader. Loading efficiencies were calculated as the ratio of fluorescence signal in supernatant over fluorescence signal of the overall suspension.

Liposome Preparation and Fusion to MSN. Lipid formulations were prepared from pure lipid stock solutions at 25 mg/mL in chloroform kept in an argon glove box. Lipid components in chloroform were mixed and chloroform was evaporated using a rotary evaporator. The obtained lipid films were then rehydrated to a concentration of 5 mg/mL in 1x PBS. The resulting liposomes were then characterized by DLS to determine hydrodynamic size and polydispersity index. Fusion of lipids to the MSN surface was done at a weight ratio of 1:5 MSN to lipids. MSN were suspended in DI H_2O at a concentration of 1 mg/mL. Liposomes were added to MSNs under sonication while pipetting up and down ~25 times. The resulting LC-MSNs were then spun down and washed once with 1x PBS.

GRP78 Ligand Conjugation Strategies. For NHS-NH_2 conjugation of GRP78, the NHS lipid film was rehydrated with a 1 mg/mL stock solution of GRP78 in 1x PBS (CPC Scientific 937657) to a final concentration of 5 mg/mL liposomes and sonicated for 30 minutes. The resulting liposomes were then fused to the surface of MSNs pre-suspended in DI H2O at a 1:5 MSN to lipid weight ratio and incubated at room temperature for 30 minutes. The resulting LC-MSNs were then spun down at 20,000 g (10 min) and resuspended in 1x PBS to a final concentration of 1 mg/ mL.

LNCaP Cell Culture and Cytotoxicity Analysis. The androgen sensitive human prostate adenocarcinoma metastatic cell line (LNCaP) was cultured in RPMI 1640 media with L-glutamine (Corning 10-040-CV) supplemented with penicillin/streptomycin (ThermoFisher 15140122) and 10% fetal bovine serum (EMD Millipore 12306C). Cell cultures were maintained at 37°C and 5% CO_2. For cytotoxicity studies, LNCaP cells were seeded in 96 well plates at 10,000 cells per well and incubated with LC-MSN system components for 24 or 48 hours. Analysis of LC-MSN cytotoxicity with the LNCaP cell line was assessed on a Biotek microplate reader using the commercially available Cell Titer Glo assay (Promega G7571) according to the manufacturer's protocol.

Confocal Microscopy Imaging. For visualization of LC-MSN cellular interactions, LNCaP cells were grown on No. 1.5 coverslips in 6 well plates at a density of 250,000 cells per well overnight. Lysotracker (Invitrogen L7528) was incubated with live cells at 50 nM according to the manufacturer's protocol. The next day, Cy3 labeled LC-MSNs were added for the indicated times to their respective wells and incubated at 37 °C. Cells were then washed twice with pre-warmed 1x PBS, fixed with 4% paraformaldehyde for 15 minutes at room temperature. Following fixation, cells were permeabilized using 0.1% Triton-X in PBS for 15 minutes. Cells were then incubated in a 1% BSA blocking buffer for 20 minutes. All cell staining solutions were prepared by diluting fluorescently conjugated antibodies in 1% BSA in PBS. Rab5a-Alexa Fluor 488 (Santa Cruz Biotechnology sc-46692) was diluted at 1:100 and incubated with cells at 4 °C overnight. Clathrin heavy chain-Alexa Fluor 475 (Invitrogen MA1-065) was diluted to 5 µg/mL and incubated with cells at 4 °C overnight. Cell samples were then rinsed twice with 1x PBS before being mounted to microscopy slides in Prolong Gold with DAPI (Thermo Fisher P36935). All microscopy images were obtained using a Leica DMi8 TCS SP8 confocal microscope. Confocal images were deconvoluted using Huygens Deconvolution software package.

Flow Cytometry Analysis of LC-MSN Uptake Kinetics. LNCaP cells were seeded in 6 well plates at 250,000 cells per well and incubated overnight at 37 °C. The next day, cells were incubated at the indicated times with 50 µg/mL Cy3 LC-MSNs. Cell samples were then washed twice with 1x PBS and collected using 0.05% Trypsin-EDTA (Thermo Fisher 25300054) before being fixed with 4% PFA in 1x PBS. Cell samples were analyzed on a Thermo Fisher Attune NxT flow cytometer.

Human Blood Hemolysis Analysis. Whole human blood was obtained from (Innovative Research, IWB1K2E10ML). Red blood cells (RBCs) were then isolated using Ficoll-Paque PLUS (Cytiva #17144002) and density gradient centrifugation at 800 xg for 8 minutes. RBCs were then purified with successive 1x PBS washing and centrifugation steps (800 xg, 8 minutes) before being suspended in 1x PBS (~ 4 x 10^6 cells/mL). Isolated RBCs were then incubated with relevant MSNs, CaMSNs or LC-CaMSNs at 37 °C for three hours. Samples were then centrifuged and resulting supernatant hemoglobin amounts were assessed via plate reader endpoint absorbance measurements (570 nm). The percentage of hemolysis for each sample was calculated using Equation 1 below. Negative control samples corresponded to RBCs suspended in 1x PBS at physiological pH while positive control samples corresponded to RBCs suspended in DI H_2O.

$$\% \, Hemolysis = \frac{Sample\ abs - Negative\ Control\ abs}{Positive\ Control\ abs - Negative\ Control\ abs} * 100 \qquad [1]$$

LNCaP mRNA Proof of Concept Experiments. LNCaP cells were seeded in 96 well plates at 10,000 cells per well and incubated overnight at 37 °C. The next day media was removed and replaced with media containing Lipofectamine/mRNA complexes or mRNA loaded LC-MSNs and incubated at 37 °C for 24 hours. Lipofectamine MessengerMax (Invitrogen LMRNA003) complexes were prepared and added to cells according to manufacturer protocol based on recommended high and low amounts of reagents.

Real-time qPCR Analysis. LNCaP cells were seeded in 6 well plates at 250,000 cells per well and incubated overnight at 37 °C. Relevant LC-CaMSNs loaded with luc-mRNA were incubated with cells (50 µg/mL) for 24 or 48 hours. RNA was then extracted using an IBI reagent Kit (IB47602, IBI Scientific, Dubuque, IA). qPCR was performed on a LightCycler 480 instrument (Roche Diagnostics, Indianapolis, IN). The mRNA level was measured by qPCR. The gene levels were normalized by 18S. Expression level changes were calculated by comparing to a non-treated control.

Luciferase F: TGCACATATCGAGGTGGACATC

Luciferase R: TGCCAACCGAACGGACAT

***Ex ovo* chick chorioallantoic membrane model (CAM) Maintenance and Analysis.** Fertilized white leghorn chicken eggs were purchased from a local farmer on embryonic developmental day zero (EDD). Eggs were placed in a GOF 1500 cabinet incubator with 60% humidity at 38 °C and allowed to rock until EDD 3. On EDD day 3, a Dremel tool equipped with a No. 5 blade was used to score the eggs along the shortest circumference. The eggs are then cracked into a sterile weigh boat. Viability of chick embryos out of the shell in the weigh boats was confirmed by observing an intact yolk and a visible heartbeat. Embryos were then covered with a square plastic petri dish cover and placed in a VWR Symphony incubator at 37 °C and 0% CO_2 until EDD 16. On EDD 16, embryonic vasculature was labelled by microinjecting LCA fluorescein (1:100, 250 µL) and allowed to circulate for 15 minutes before microinjecting Cy3 labeled LC-MSNs. Embryos were then imaged using a Zeiss Axio Examiner Z1 microscope. All experiments were conducted in accordance with the regulations and guidelines of the Institutional

Animal Care and Use Committee at the University of New Mexico (IACUC Protocol # 21-201149-T-MC).

Mouse Models and *in vivo* Experimentation. Adult male NOD scid gamma (NSG) mice at the University of New Mexico were maintained on a 12-hour light-dark cycle with *ad libitum* access to food and water. Animals were group housed and all experiments were conducted in accordance with the regulations and guidelines of the Institutional Animal Care and Use Committee at the University of New Mexico (IACUC Protocol # 22-201155). LC-MSNs were administered to adult male NOD scid gamma (NSG) mice via retro-orbital injections under isoflurane anesthesia (1 mg/mL, 100μL). For xenograft establishment in NSG mice, LNCaP cells were suspended to a final concentration of 5×10^7 cells/mL in serum free, phenol red free RPMI media. Cell suspensions were then mixed at 50% volume with phenol red free Matrigel (Corning 356237) before subcutaneous injection in the right flank (200 μL final injection volume). Tumor growth was monitored serially over time. Fluorescent LC-MSN and bioluminescence signal was tracked in mice using a Perkin Elmer IVIS Spectrum *in vivo* imaging system.

3. Results and Discussion

3.1 MSN Morphology and Pore Size Modulation. MSNs in this study were synthesized via a sol gel surfactant template approach in which a silica precursor (TEOS) is condensed over an aqueous surfactant self-assembly (Figure 1a). This approach is attractive for engineering nanocarriers due to its ease of synthesis as well as the high level of control over reaction products.[32] The interchanging of surfactants, conditions of the reaction scheme and varying additions of the silica precursor enabled the creation of a library of MSNs having varying morphologies and pore sizes as for subsequent tailoring to nucleic acid cargos. First, hexagonal MSNs having a 2nm pore size structure were synthesized via CTAB templating base catalyzed by NH_4OH according to previous work.[33] Secondly, spherical MSNs having either dendritic or worm-like pores were synthesized using a biphasic reaction setup adapted from our previous work.[34] All synthesis approaches resulted in highly monodisperse nanoparticle populations based on the low polydispersity indices ($PDI \leq 0.2$) obtained from DLS measurements of resulting reaction batches (Figure 1b). The DLS zeta potential measurements of the synthesized nanoparticles (-28.9 ±2.4 mV) were indicative of a pure silica matrix in water (Figure 1c). TEM indicated highly ordered resulting mesoporous structures for the hexagonal (Figure 1d, left), 5nm wormlike (Figure 1d, middle) and 8nm dendritic nanoparticles (Figure 1d, right).

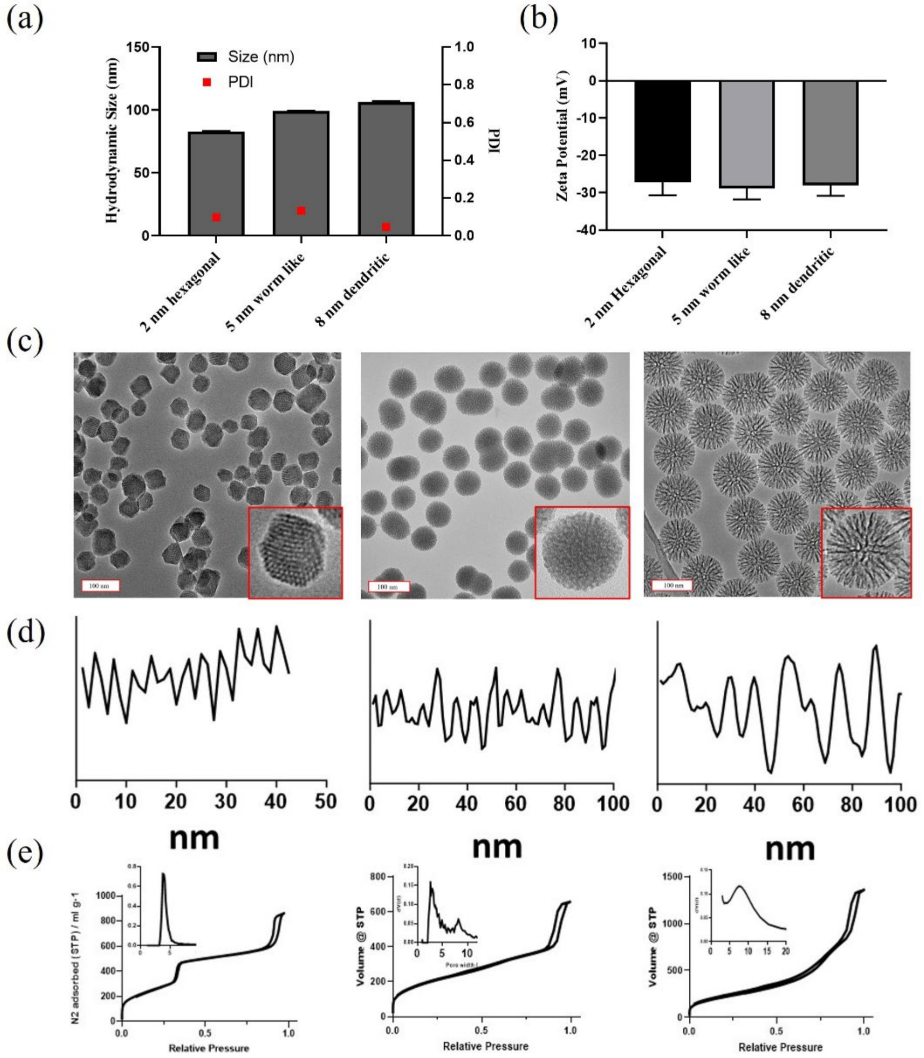

Figure 1. MSN pore size and morphology modulation. (a) DLS measurement results for size and PDI of as synthesized MSNs, (b) DLS measurement results for zeta potentials of as synthesized MSNs (c) Representative TEM images of as synthesized MSNs left: 2 nm hexagonal middle: 5nm worm like right: 8 nm dendritic MSNs, insets are zoomed in images to demonstrate morphology, (d) Profile topography of hexagonal (left), worm like (middle) or dendritic (right) MSNs (e) Nitrogen adsorption isotherms for hexagonal (left), worm like (middle) or dendritic (right) MSNS inset indicate pore size distribution.

3.2. Metallic Entrapment for MSN Loading of Nucleic Acids.

.2.1. siRNA Loading and Pore Entrapment. Engineering of chemical and physical characteristics for improved siRNA or mRNA loading into silica mesopores must also consider the need for efficient release kinetics and biocompatibility within biological systems. Additionally, reducing the complexity of such systems boosts their reproducibility as well as streamlines future use in clinical settings. To avoid the reliance on cationic polymers, cationic lipids or additional surface functionalization, we have shown that the utilization of metal cations can link silanolate (Si-O$^-$) groups and negatively charged nucleotides by overcoming electrostatic repulsive forces. We hypothesized that complexation between nucleic acid molecules, metal cations and silanolate groups on the surface of the silica nanoparticles and within the pores would enhance siRNA or mRNA loading into negatively charged MSN mesopores and that the resulting complexation would serve to trap nucleic acids within the pores (Figure 2a).

Impact of MSN morphology/pore size. In order to evaluate surface morphology impact on nucleic acid loading using metallic cations, we have adapted a previously reported procedure that uses high concentration of calcium chloride to load siRNA into porous silicon by forming insoluble calcium silicate species.[31] As expected, bare MSNs loaded negligible siRNA amount, due to natural electrostatic repulsion while the use of the 4M $CaCl_2$ solution drastically increased the loading efficiency with a ratio 1/0.75/0.5 as a function of pore size.(Figure 2b). These results suggest a dependence on MSN pore size and morphology for calcium mediated loading of siRNA.

Evaluation of siRNA loading in function of cation radius and solution pH. We then hypothesized that the loading extent of siRNA could be further modulated as a function of ionic radii of the cations. To test this hypothesis, we used Mg^{2+} (ionic radius=72 pm), Ca^{2+} (Ca^{2+} = 100 pm), Na^+ (ionic radius=102 pm), and K^+ (ionic radius=138 pm) in 4 M cation chloride solutions to load fluorescent siRNA. Loading efficiency (<10%) results along with zeta potential measurements (~ -20 mV, with no difference compared to bare MSN) indicated ineffective loading with monovalent cations (Na^+, K^+) in both acidic and basic pH conditions, in contrast to an effective loading (>80%, pH 9.5) with divalent cations (Mg^{2+}, Ca^{2+}) ruling out the effect of the ionic radius effect in favor of the cation valency. Additionally, it is noteworthy that acidic pH reduced to 30% the loading efficiency using divalent cations (Figure 2d, 2f) implying that pH and hence, the degree of ionization of both silanols and phosphate (nucleotide), plays a key role in the metallic entrapment process. Considering the Hendersson Hasselbach relationship ($pH= pKa +\log[A^-]/[AH]$), the ratio of both base/acid couples $SiO^-/SiOH$ and PO_4^-/ PO_4H groups will drastically evolve from ~ 20 at pH=3.5 to ~10^7 at pH=9.5 suggesting that an electrostatic link plays a key role in the metallic entrapment process. Our results from STEM imaging do not show any morphological or contrast difference of MSN incubated with and without concentrated $CaCl_2$ (Figure 2e), as previously shown with the silicon surface in a reported study.[31] These results suggest a nucleic acid entrapment strategy via an electrostatic metallic link without formation of observable silicate precipitate.

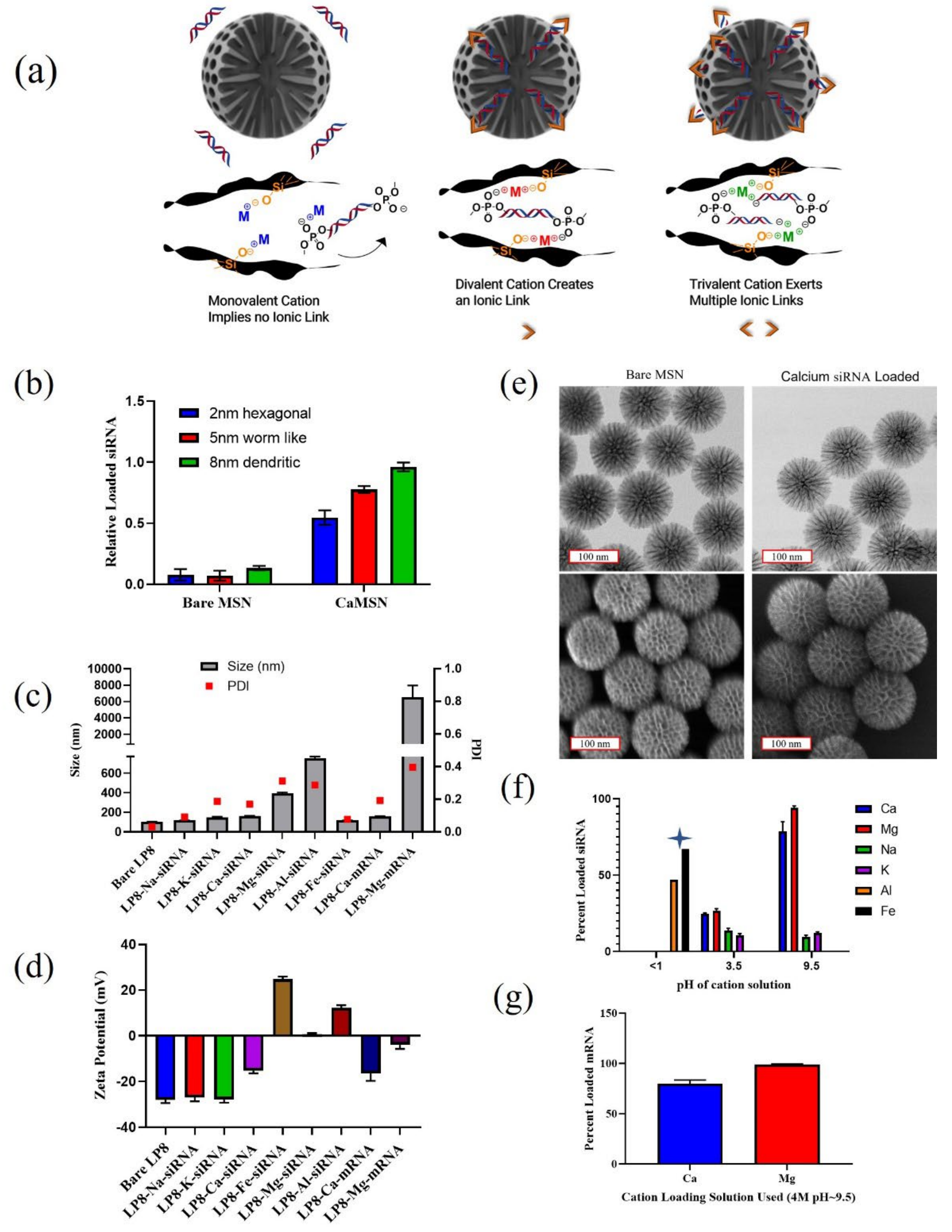

Figure 2. Metal based cation loading of siRNA or mRNA. (a) Schematic showing cation loading and entrapment of RNA (b) Initial siRNA loading as a function of pore size and morphology. pH=4.5 (c) DLS characterization of resulting cation loaded MSNs (d) DLS characterization of zeta potential for resulting cation loaded MSNs (e) STEM images of siRNA loaded MSNs (f) Cation siRNA loading efficiencies, blue star indicates cation loading solutions not applicable to pH adjustments (g) Cation mRNA loading efficiencies.

We then extended the loading procedure to other cations having higher valences. Prepared 4 M solutions of $FeCl_3$ and $AlCl_3$ resulted in pH <1. Adjusting the pH to >3 resulted in important precipitation on a wide range of concentrations (0.04 M-0.4 M) (Figure S1). The obtained loading efficiency results (at unadjusted pH<1) for trivalent cations (Fe^{3+}, Al^{3+}) also indicated relatively good loading (~80%), however these conditions would create technical challenges and would not be applicable to therapeutically relevant nucleic acids.

We then sought to understand the interaction between the silica surface and siRNA/cation complexes with a hypothesis that the state of silanol groups would play a key role in the ability of calcium loading to occur. To test this hypothesis, we conducted fluorescent tracking of siRNA loading utilizing $CaCl_2$ solutions at a higher pH (pH~9.5). In respect to our hypothesis, at higher pH the siRNA loading efficiency was increased to approximately 80% (Figure 2f). This is likely due to the fact that at lower pHs, the silanol groups on the surface are protonated (SiOH), inhibiting optimal interaction with cation/siRNA complexes. At pHs well above the pKa of silanol groups we expect the surface to be significantly deprotonated, facilitating effective interactions between $Si\text{-}O^-$ groups and cation/siRNA complexes.

3.2.2 Metallic entrapment efficiently loads messenger RNA. After confirming the capability of divalent metallic cations to entrap siRNA (~50 nucleotides, double stranded), we wanted to evaluate the efficacy of this strategy with mRNA, a significantly larger molecule (1921 nucleotides, single stranded) with comparable chemistry. The loading data shows 85-100% loading efficiency, suggesting that divalent cations can exert the same effect on the mRNA nucleotides and assist by folding mRNA within the pores. The ability of divalent cation loading was also applicable to mRNAs as indicated by results from tracking of a fluorescent Firefly Luciferase mRNA (Figure 2g). DLS measurement results for cation loaded MSNs indicated optimal hydrodynamic size (<200 nm) and PDI (<0.2) of the CaMSN and was therefore chosen for subsequent experimentation (Figure 2c). STEM imaging results after Ca^{2+} loading indicated that nucleic acids are loaded into pores and that MSN morphology is retained (Figure 2e). Finally, EDS elemental analysis of nucleic acid loaded CaMSNs confirmed the presence of calcium and phosphorous attributed to the phosphate backbone of the siRNA (Figure S2). Considering these results, we decided to move forward with the calcium rich MSN (CaMSN) as divalent cations showed optimal loading conditions compared to mono and trivalent metallic ions, and Ca-MSN exhibited optimal stability as compared to Mg-MSN.

3.3 Fusion of Liposomes to MSN for LC-MSN Formation. The addition of liposomes to coat the CaMSN was hypothesized to enhance nanoparticle biocompatibility, improve nanoparticle stability within biologically relevant medias as well as provide a modifiable surface for subsequent functionalization for targeting within the aggressive LNCaP cell model of PC (Figure 3a). Table 1 in the Supplemental Information lists the liposomal formulations developed in this study. The colloidal stability of neutral and GRP78 encapsulated CaMSNs was confirmed by DLS measurements where the full LC-CaMSN construct and its individual components remained in the 150-200 nm range with a low polydispersity indices (PDI<0.2) indicating homogeneous nanoparticles (Figure 3b). DLS zeta potential measurement results further indicated successful encapsulation of CaMSNs (Figure 3c). The addition of liposomes to coat the metallic enhanced MSN was also hypothesized to enhance the resistance of $SiO\text{-}M\text{-}PO_4$(nucleotide) to other ionic species that can overlap with the nucleotide's phosphate. For instance, incubating siRNA-CaMSN

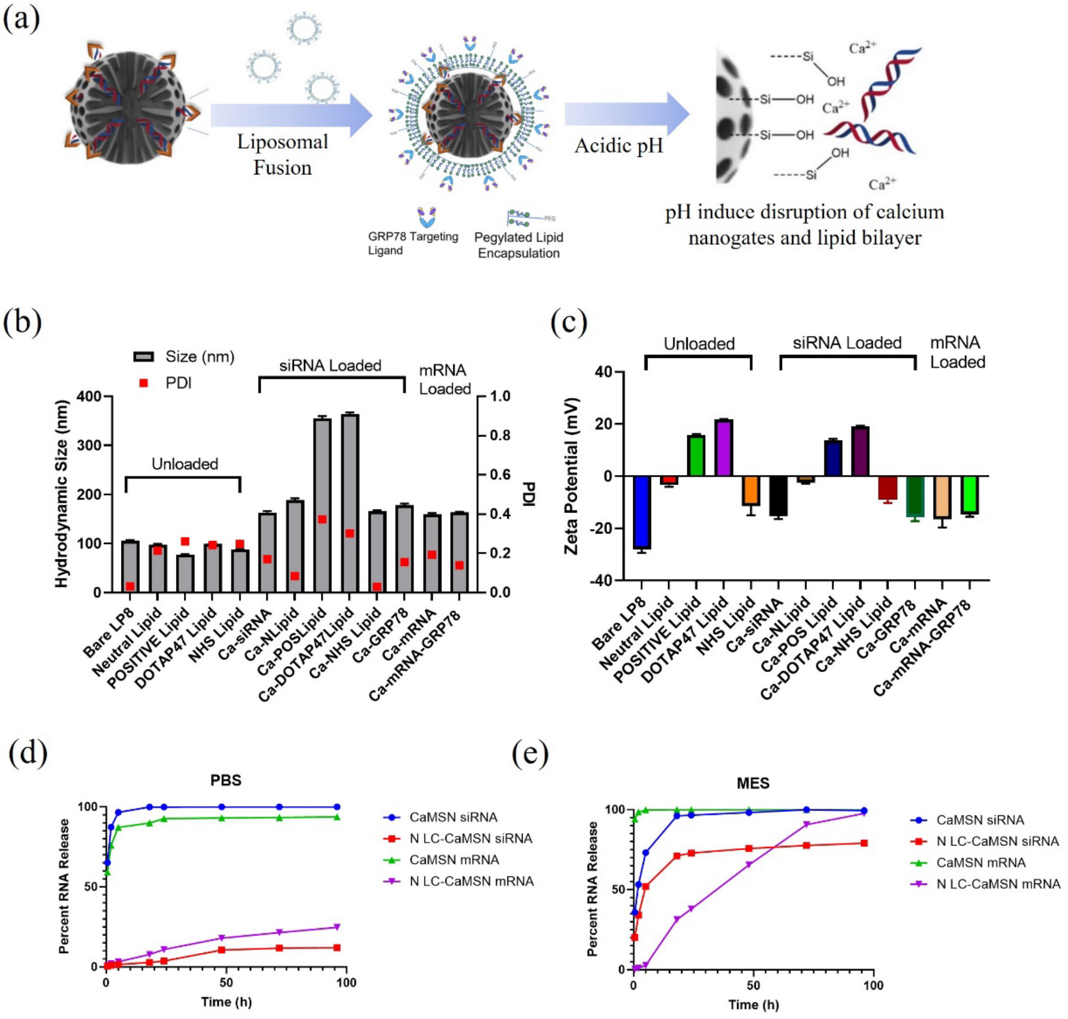

Figure 3. Lipid encapsulation of CaMSN loaded with RNA. (a) Schematic of lipid coating of calcium MSN and pH-sensitive release mechanism. (b) DLS characterization LC-CaMSN construct and components. (c) DLS characterization of zeta potential of LC-CaMSN construct and components. (d) Release kinetics for RNA loaded CaMSN or LC-CaMSN incubated in 1x PBS. (e) Release kinetics for RNA loaded CaMSN or LC-CaMSN incubated in MES.

in PBS resulted in a brutal release of the nucleic acid (100% within 30 min) due to the replacement of siRNA's phosphate groups by the free and labile phosphate from PBS or sulfates in the case of the endosomal mimicking solution, MES (Figure 3d). The lipid coating does not affect the loading of the nucleic acid meaning that lipid protection of the metallic entrapments occurs faster than their destabilization resulting from PBS. To confirm this, we tracked the release of fluorescently labeled siRNA or mRNA in PBS and an endosomal mimicking solution (MES) for 4 days. Significant release of siRNA was observed (up to 80%) within MES while release within PBS having a physiological pH was minimal (< 15%) (Figure 3e). DLS hydrodynamic size measurement results indicated that lipid encapsulation conferred superior stability properties of neutral LC-CaMSNs over bare CaMSNs for up to 4 days in PBS and complete cell media (Figure S3). LC-CaMSNs incubated in pure serum degraded over time agreeing with our previous work.[17] LC-CaMSNs incubated in MES exhibited instability, further supporting a pH triggered disruption and subsequent release of nucleic acids (Figure S3). Further confirmation of successful lipid coating of RNA loaded CaMSNs was enabled via cryogenic electron microscopy. The lipid coating appears as a distinct halo ring surrounding the dendritic MSN (Figure S4).

3.4 LC-CaMSN Interactions with LNCaP PC cell line and Human Red Blood Cells. The LC-CaMSNs were then introduced to the LNCaP cell line for *in vitro* analysis. The biocompatibility of the LC-MSN system was analyzed using the Cell Titer Glo® assay in which cell viability is characterized based on the presence of ATP, signaling metabolically active cells. After 48 hours of incubation with a LC-CaMSN having a neutral lipid coating, no significant reduction in cell viability was observed, indicating encapsulation with neutrally charged lipids may reduce cytotoxic effects of the bare MSNs (Figure 4c). To further assess the biocompatibility of the LC-CaMSN system within the bloodstream, we then tested the hemolytic activity of particles incubated with human red blood cells for 3 hours at 37 °C. Bare MSNs caused significant hemolysis regardless of the concentration compared to bare CaMSNs which exhibited slightly less hemolysis likely due to incomplete covering of silanol groups with calcium (Figure 4a). CaMSNs coated with either neutral lipids or GRP78 lipids exhibited significantly less hemolytic activity (Figure 4a), further supporting the use of lipid coatings for enhancement of biocompatibility. Cellular uptake kinetics for non-targeted (Figure S6 a) or targeted (Figure 4b) were evaluated by flow cytometry. Representative gating parameters used to determine the percentage uptake for flow cytometry experiments are given in Figure S6. In the case of non-targeted LC-CaMSNs, rapid uptake was observed for positively charged particles as compared to neutrally charged particles, most likely due to nonspecific electrostatic interactions with cellular membranes. GRP78 minibody targeted particles exhibited superior uptake kinetics, indicating the need for active targeting strategies in the LNCaP cell line to achieve rapid uptake in cancerous cells.

The majority of nanoparticle systems are internalized within cells via endocytotic pathways in which nanoparticles are trapped in vesicles (endosomes) which are trafficked to lysosomes for hydrolytic enzyme degradation.[35,36] We first investigated the neutral lipid LC-CaMSN uptake by flow cytometry and confocal microscopy. Flow cytometry (Figure 4b) and confocal microscopy (Figure 4f) results showed full association and internalization within cells at 48h. In line with studies that confirmed the capacity of cells to readily uptake positively charged nanoparticles, we then evaluated our LC-CaMSN having positive liposomal encapsulations, namely POSITIVE and DOTAP47 (inspired by our previous work) with which internalization via endocytosis was previously demonstrated in HeLa and A549 cells.[17] Confocal microscopy data showed a significant amount of nanoparticles associated with LNCaP cells at 2 hours (Figure S7 and Figure S8). Deconvoluted 3D rendered images obtained from z-stack confocal imaging further demonstrated internalization of the POSTIVE or DOTAP47 LC-MSNs with or without calcium by 6 hours (Figure S9 and Figure S10). Additionally, POSITIVE or DOTAP47 LC-MSNs colocalized (yellow areas, Pearson correlation coefficient PCC = 0.5236) with the early endosomal marker Rab5 at 6 hours, supporting an internalization mechanism via endocytosis (Figure 4f). We hypothesized that the addition of calcium to LC-MSNs would not only load RNAs but could also provide an endosomal escape release mechanism. Endosomal escape was assessed by tracking colocalization between Rab5 (early endosomes) and LC-MSNs or LC-CaMSNs via confocal microscopy. At 24 hours, deconvoluted confocal microscopy images revealed that LC-CaMSNs colocalized less with Rab5 as compared to LC-MSNs lacking calcium, supporting calcium's role in endosomal escape (Figure 4f). To further support qualitative confocal imaging, colocalization was quantified by tracking Pearson correlation coefficients (PCC) between Rab5 and LC-MSNs or LC-CaMSNS as a function of incubation time with LNCaP cells. Results demonstrated LC-CaMSNs internalized via endocytosis escaped endosomes more quickly or completely as compared to LC-MSNs lacking calcium (Figure S11). Glucose Receptor Protein 78 KDa (GRP78) has been previously established as an overexpressed receptor on LNCaP cells, and has been previously

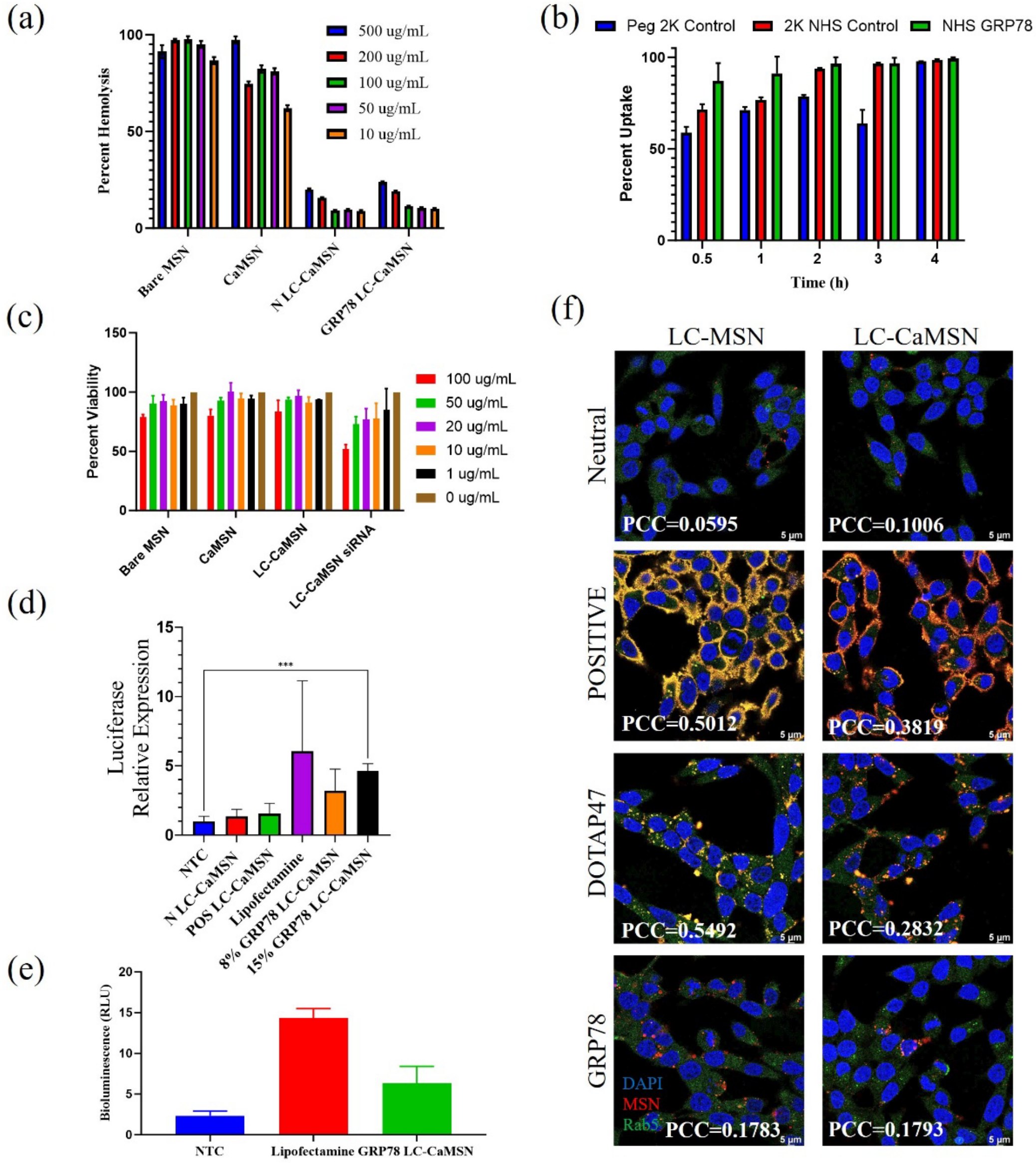

Figure 4. In vitro analysis results of LC-CaMSN and LNCaP or human RBC interactions. (a) Calculated percent hemolysis as a function of MSN or LC-CaMSN concentration, (b) Flow cytometry analysis of cells following incubation with targeted LC-CaMSN (c) Cytotoxicity analysis of 72-hour incubation with MSN and LC-MSN (d) Quantitative RT-PCR analysis results for luciferase mRNA delivery. (e) Plate reader results of cell bioluminescence following 24h LC-CaMSN incubation. (f) Deconvoluted confocal images of LNCaP cells following 24h incubation with LC-MSNs having various lipid coating with or without calcium using a 63x oil immersion objective. Scale bars indicate 5 μm.

validated as a functional molecular moiety for targeted delivery systems in PC therapeutic applications.[37,38] We hypothesized that LC-MSNs with or without calcium that are functionalized with a GRP78 minibody would enable quick association with LNCaP cells. Flow cytometry results confirmed almost complete uptake of GRP78 LC-CaMSNs within 30 minutes of incubation at 37 °C (Figure 4b). Additionally, GRP78 functionalized LC-MSN or LC-CaMSN systems lacked colocalization with Rab5 (Figure 4f, Figure S7 and Figure S8) suggesting an alternative internalization pathway. 3D rendered confocal images of LC-MSN or LC-CaMSNs following incubation with LNCaP cells confirmed internalization by 2 hours (Figure S9 and Figure S10). To confirm that GRP78 functionalization results in LC-MSN or LC-CaMSN binding to surface expressed GRP78 exclusively, we pre-incubated LNCaP cell with free GRP78 (insert concentration) for 4 hours before incubating cells with LC-CaMSNs. Deconvoluted confocal microscopy results demonstrated a lack of LC-CaMSN association or internalization supporting that GRP78 functionalized LC-CaMSNs bind exclusively to surface expressed GRP78 (Figure S12).

Successful delivery of mRNA within the LNCaP cell line was first assessed via quantitative RT-PCR after cells were incubated with various LC-CaMSNs. The commercially available *in vitro* transfection agent Lipofectamine MessengerMax® was used as a positive control. Results indicated that as compared to the non-treated control, GRP78 targeted LC-CaMSNs significantly delivered more mRNA to cells and that the relative gene expression could be increased with increasing amount of NHS within the lipid formulation (Figure 4?) We then assessed subsequent protein expression after mRNA delivery in LNCaP cells via expression of luciferase and subsequent bioluminescence as measured by plate reader. Similarly to RT-PCR results, better bioluminescence expression was observed in cells incubated with targeted LC-CaMSN systems (Figure 4d). While Lipofectamine® outperformed the LC-CaMSNs as far as bioluminescence signal, cytotoxicity analysis in which volumes of LC-CaMSN and Lipofectamine® were matched revealed that Lipofectamine® was significantly more toxic than the LC-CaMSN carrier. (Figure S13). This indicates that Lipofectamine® would not be appropriate as a therapeutic delivery agent and should only serve as a control for experiments.

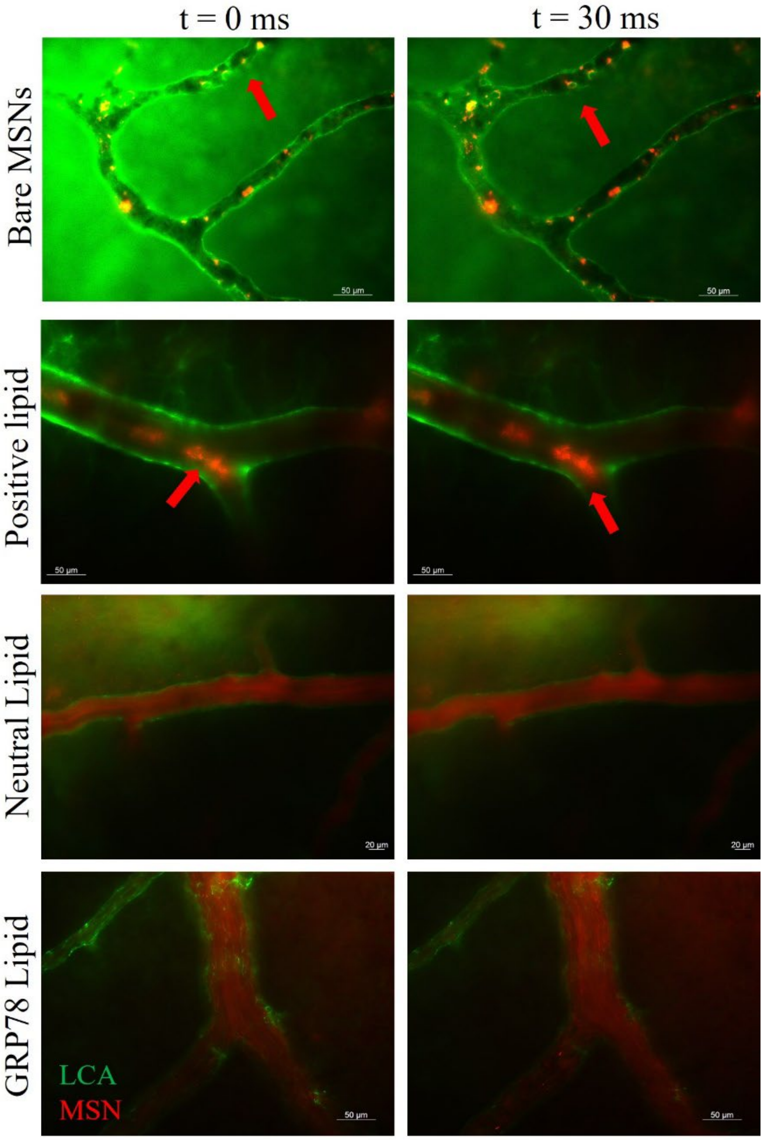

Figure 5. Timelapse images of LC-MSN circulation within CAM vasculature taken at 40x. Red arrows indicate MSN aggregation.

3.6 LC-MSN system vascular margination, circulation and stability within *ex ovo* chick chorioallantoic membrane model (CAM). The CAM can be classified as a bridge between *in vitro* and *in vivo* systems making it an ideal biological barrier platform for evaluating vascular margination, binding, circulation time and stability of the LC-MSN system.[39] Bare CaMSNs and LC-CaMSNs having varying liposomal coatings were injected into CAM vasculature and imaged after allowing 20 minutes of circulation (Figure S7). Bare MSNs were observed to aggregate and bind to vasculature walls (Figure 5) and remaining non-aggregated MSNs were observed to quickly be removed from circulation most likely via innate immune system opsonization.[40] LC-CaMSNs having a positive charge (POSITIVE) exhibited relatively longer circulation within CAM vasculature but were quickly bound to vasculature walls and red blood cells most likely due to electrostatic interactions between negatively charged membranes and the positively charged LC-CaMSN (Figure 5). Additionally, positively charged LC-CaMSNs ultimately exhibited aggregation. Finally, neutrally charged LC-CaMSNs with or without the GRP78 targeting ligand exhibited stable circulation, no vasculature binding, and no apparent reduction in circulation due to opsonization (Figure 5). Videos of LC-CaMSN live circulation within the CAMs are provided in supplemental information of online version.

3.7 LC-CaMSN *in vivo* Tumor Retention. We tested the retention of DyLight 633 labeled LC-CaMSNs after subcutaneous (SC) injections within NSG mice engrafted with LNCaP tumors for up to 48 hours. Whole live animal IVIS imaging results for SC injected LC-CaMSNs indicated superior retention at the tumor site in the case of GRP78 LC-CaMSNs as compared to non-targeted N LC-CaMSNs (Figure 6a). After live animal imaging, mice were euthanized and necropsied to assess LC-CaMSN presence in organs and tumors. Enhanced tumor retention in the case of GRP78 targeted LC-CaMSNs as compared to non-targeted neutral LC-CaMSNs was confirmed via quantification of Dylight 633 LC-CaMSN signal in dissected organs and tumors (Figure 6b). IVIS images of necropsied organs upon which this quantification were carried out over are given in Figure S15.

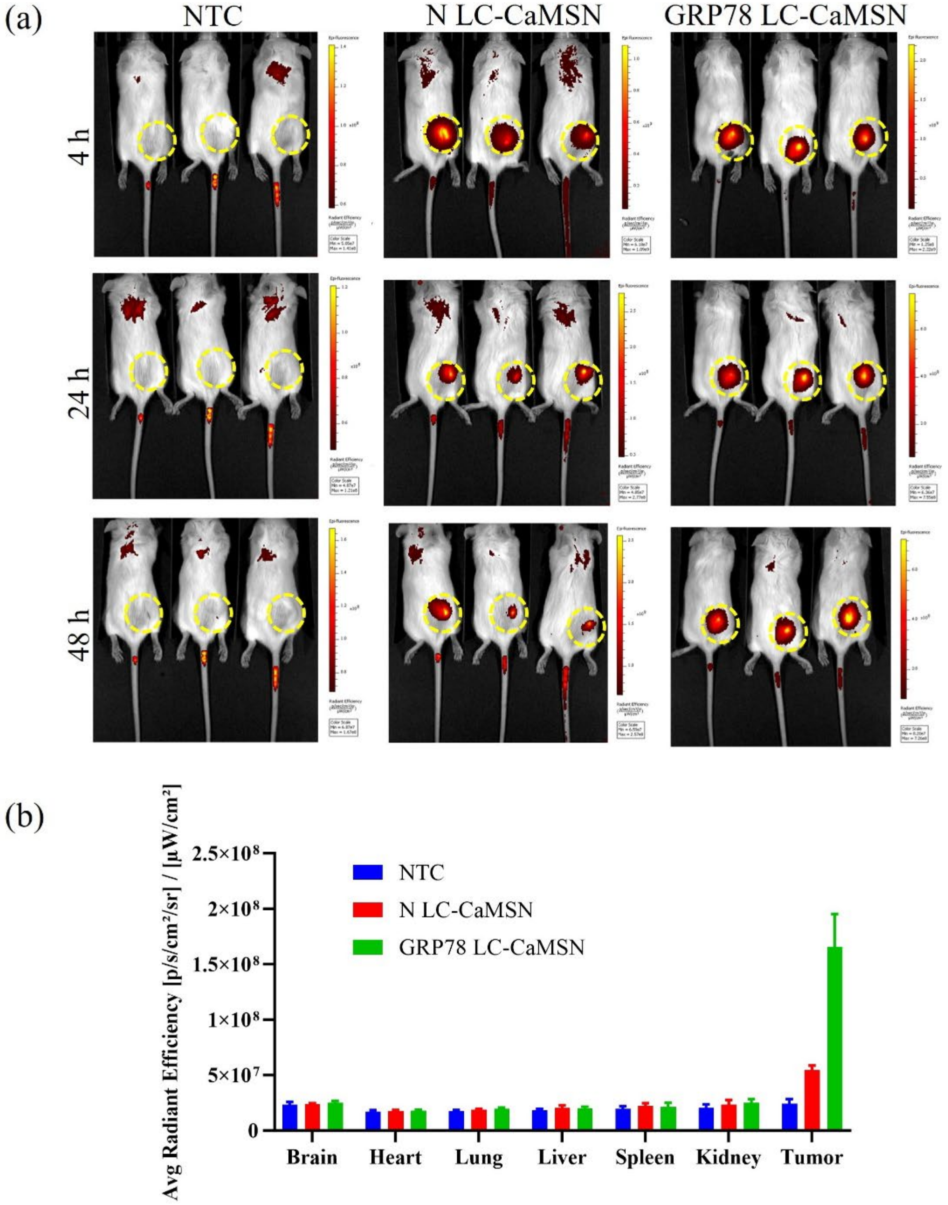

Figure 6. Imaging of NSG mouse LNCaP xenografts obtained from IVIS imaging system after right flank subcutaneous Dylight 633 mRNA loaded LC-CaMSN injections. (a) Whole body live images of dorsal side of mice. Dashed yellow lines indicate tumor site. (b) Quantification of fluorescent signal in mouse organs dissected 48 hours after injections.

4. Conclusions. In summary we have presented the development and characterization of a lipid coated mesoporous silica nanoparticle that is capable of loading either siRNA or mRNA via metal cation complexation. To the best of our knowledge this is the first report of successful mRNA loading using metallic cation mediated entrapment. We demonstrated colloidally stable constructs that exhibit pH triggered release for endosomal escape within LNCaP cells. *Ex ovo* results supported the biocompatibility of the system along with promising stability and circulation characteristics. The inclusion of calcium cations to the LC-MSN system provided an enhanced endosomal escape mechanism as seen by confocal microscopy. The tailorable and biocompatible nature of the LC-CaMSN along with high loading efficiencies for siRNA and mRNA allowed for the addition of tumor retention ligands as shown in the intratumoral retention of the GRP78 LC-CaMSN. Future work will be focused on the systematic investigation of fine-tuning liposomal formulations and GRP78 conjugation strategies for CaMSN encapsulation for optimized tumor accumulation upon IV administration and subsequent reduction of tumor burden.

Supporting Material Available: Table of liposomal formulations, picture of $FeCl_3$ solutions and corresponding Fe loaded MSNs, EDS elemental analysis of siRNA loaded MSNs, DLS hydrodynamic size characterization of bare or lipid encapsulated CaMSN incubated in various physiological solutions, Cryo-EM images of LC-CaMSNs, Analysis of LC-CaMSN hemolysis, Representative flow cytometry gating parameters, 2D and 3D surface-rendered deconvoluted confocal images of LNCaP cells, Graph of PCC for LC-CaMSN colocalization with Rab5, Deconvoluted confocal images of GRP78 pre-incubated LNCaP cells, Cytotoxicity of Lipofectamine® results, CAM injection of LC-MSNS imaging setup, Necropsied IVIS images of mice organs and tumors.

Author Information

Corresponding Authors

Angelea Maestas-Olguin- *Department of Chemical and Biological Engineering, University of New Mexico, Albuquerque, NM, United States* Email: angemaestas13@unm.edu

Achraf Noureddine- *Department of Chemical and Biological Engineering, University of New Mexico, Albuquerque, NM, United States* Email: anoureddine@unm.edu

C. Jeffrey Brinker- *Department of Chemical and Biological Engineering, University of New Mexico, Albuquerque, NM, United States* Email: jbrinker@unm.edu

Notes

The authors declare no competing financial interest.

Acknowledgements

This material is based upon work supported by the National Science Foundation Graduate Research Fellowship under Grant No. 1939267. Research reported in this publication was supported by the National Cancer Institute of the National Institutes of Health under award number RO1CA22653701. We gratefully acknowledge the use of the UNMCCC Animal Models, Fluorescence Microscopy, Flow Cytometry Shared Resources as well as the NIH P30CA118100 grant that supports the UNMCCC and these shared resources. We would like to thank the University of New Mexico Office of the Vice President for Research for the WeR1 Faculty Success Program funding and the Center for Metals and Biology and Medicine pilot funding from P20GM130422-03. This work was performed, in part, at the Center for Integrated Nanotechnologies, an Office of Science User Facility operated for the U.S. Department of Energy (DOE) Office of Science. Sandia National Laboratories is a multimission laboratory managed and operated by National Technology & Engineering Solutions of Sandia, LLC, a wholly owned subsidiary of Honeywell International, Inc., for the U.S. DOE's National Nuclear Security Administration under contract DE-NA-0003525. The views expressed in the article do not necessarily represent the views of the U.S. DOE or the United States Government. This work was performed, in part, at the Center for Integrated Nanotechnologies, an Office of Science User Facility operated for the U.S. Department of Energy (DOE) Office of Science. Los Alamos National Laboratory, an affirmative action equal opportunity employer, is managed by Triad National Security, LLC for the U.S. Department of Energy's NNSA, under contract 89233218CNA000001.

References

(1) Gandhi, J.; Afridi, A. The Molecular Biology of Prostate Cancer: Current Understanding and Clinical Implications. *Prostate Cancer and Prostatic Diseases* **2018**, *21* (1), 22.

(2) Viswanathan, S. R.; Ha, G.; Hoff, A. M.; Wala, J. A.; Carrot-Zhang, J.; Whelan, C. W.; Haradhvala, N. J.; Freeman, S. S.; Reed, S. C.; Rhoades, J.; Polak, P.; Cipicchio, M.; Wankowicz, S. A.; Wong, A.; Kamath, T.; Zhang, Z.; Gydush, G. J.; Rotem, D.; Love, J. C.; Getz, G.; Gabriel, S.; Zhang, C.-Z.; Dehm, S. M.; Nelson, P. S.; Van Allen, E. M.; Choudhury, A. D.; Adalsteinsson, V. A.; Beroukhim, R.; Taplin, M.-E.; Meyerson, M. Structural Alterations Driving Castration-Resistant Prostate Cancer Revealed by Linked-Read Genome Sequencing. *Cell* **2018**, *174* (2), 433–447.

(3) Varambally, S.; Yu, J.; Laxman, B.; Rhodes, D. R.; Mehra, R.; Tomlins, S. A.; Shah, R. B.; Chandran, U.; Monzon, F. A.; Becich, M. J.; Wei, J. T.; Pienta, K. J.; Ghosh, D.; Rubin, M. A.; Chinnaiyan, A. M. Integrative Genomic and Proteomic Analysis of Prostate Cancer Reveals Signatures of Metastatic Progression. *Cancer Cell* **2005**, *8* (5), 393–406.

(4) Monteith, G. R. Prostate Cancer Cells Alter the Nature of Their Calcium Influx to Promote Growth and Acquire Apoptotic Resistance. *Cancer Cell* **2014**, *26* (1), 1–2.

(5) Knudsen, K. E.; Penning, T. M. Partners in Crime: Deregulation of AR Activity and Androgen Synthesis in Prostate Cancer. *Trends in Endocrinology & Metabolism* **2010**, *21* (5), 315–324.

(6) Takeda, D. Y.; Spisák, S.; Seo, J.-H.; Bell, C.; O'Connor, E.; Korthauer, K.; Ribli, D.; Csabai, I.; Solymosi, N.; Szállási, Z.; Stillman, D. R.; Cejas, P.; Qiu, X.; Long, H. W.; Tisza, V.; Nuzzo, P. V.; Rohanizadegan, M.; Pomerantz, M. M.; Hahn, W. C.; Freedman, M. L. A Somatically Acquired Enhancer of the Androgen Receptor Is a Noncoding Driver in Advanced Prostate Cancer. *Cell* **2018**, *174* (2), 422–432.

(7) Klezovitch, O.; Chevillet, J.; Mirosevich, J.; Roberts, R. L.; Matusik, R. J.; Vasioukhin, V. Hepsin Promotes Prostate Cancer Progression and Metastasis. *Cancer Cell* **2004**, *6* (2), 185–195.

(8) Kara, G.; Calin, G. A.; Ozpolat, B. RNAi-Based Therapeutics and Tumor Targeted Delivery in Cancer. *Advanced Drug Delivery Reviews* **2022**, *182,* 114-113.

(9) Shugang Qin; Xiaoshan Tang; Yuting Chen; Kepan Chen; Na Fan; Wen Xiao; Qian Zheng; Guohong Li; Yuqing Teng; Min Wu; Xiangrong Song. MRNA-Based Therapeutics: Powerful and Versatile Tools to Combat Diseases. *Signal Transduction and Targeted Therapy* **2022**, *7* (1), 1–35.

(10) Zhou, Z.; Liu, X.; Zhu, D.; Wang, Y.; Zhang, Z.; Zhou, X.; Qiu, N.; Chen, X.; Shen, Y. Nonviral Cancer Gene Therapy: Delivery Cascade and Vector Nanoproperty Integration. *Advanced Drug Delivery Reviews* **2017**, *115*, 115–154.

(11) Samaridou, E.; Heyes, J.; Lutwyche, P. Lipid Nanoparticles for Nucleic Acid Delivery: Current Perspectives. *Advanced Drug Delivery Reviews* **2020**, *154–155*, 37–63.

(12) Akinc, A.; Maier, M. A.; Manoharan, M.; Fitzgerald, K.; Jayaraman, M.; Barros, S.; Ansell, S.; Du, X.; Hope, M. J.; Madden, T. D.; Mui, B. L.; Semple, S. C.; Tam, Y. K.; Ciufolini, M.; Witzigmann, D.; Kulkarni, J. A.; van der Meel, R.; Cullis, P. R. The Onpattro Story and the Clinical Translation of Nanomedicines Containing Nucleic Acid-Based Drugs. *Nat. Nanotechnol.* **2019**, *14* (12), 1084–1087.

(13) Hou, X.; Zaks, T.; Langer, R.; Dong, Y. Lipid Nanoparticles for MRNA Delivery. *Nature Reviews Materials* **2021**, *6* (12), 1078–1094.

(14) Tenchov, R.; Bird, R.; Curtze, A. E.; Zhou, Q. Lipid Nanoparticles-From Liposomes to MRNA Vaccine Delivery, a Landscape of Research Diversity and Advancement. *ACS Nano* **2021**, *15* (11), 16982–17015.

(15) Kulkarni, J. A.; Witzigmann, D.; Chen, S.; Cullis, P. R.; van der Meel, R. Lipid Nanoparticle Technology for Clinical Translation of SiRNA Therapeutics. *Accounts of chemical research*. ACS AMERICAN CHEMICAL SOCIETY: United States January 1, 2019, pp 2435–2444.

(16) Allen, T. M.; Cullis, P. R. Liposomal Drug Delivery Systems: From Concept to Clinical Applications. *Advanced Drug Delivery Reviews* **2013**, *65* (1), 36–48.

(17) Noureddine, A.; Maestas-Olguin, A.; Saada, E. A.; LaBauve, A. E.; Agola, J. O.; Baty, K. E.; Howard, T.; Sabo, J. K.; Espinoza, C. R. S.; Doudna, J. A.; Schoeniger, J. S.; Butler, K. S.; Negrete, O. A.; Brinker, C. J.; Serda, R. E. Engineering of Monosized Lipid-Coated Mesoporous Silica Nanoparticles for CRISPR Delivery. *Acta Biomaterialia* **2020**, *114*, 358–368.

(18) Croissant, J. G.; Fatieiev, Y.; Almalik, A.; Khashab, N. M. Mesoporous Silica and Organosilica Nanoparticles: Physical Chemistry, Biosafety, Delivery Strategies, and Biomedical Applications. *ADVANCED HEALTHCARE MATERIALS* **2018**, *7* (4), 1700831.

(19) Yang, Y.; Zhang, M.; Song, H.; Yu, C. Silica-Based Nanoparticles for Biomedical Applications: From Nanocarriers to Biomodulators. *Acc. Chem. Res.* 2020, *53* (8), 1545–1556

(20) Lei, Q.; Guo, J.; Noureddine, A.; Wang, A.; Wuttke, S.; Brinker, C. J.; Zhu, W. Sol-Gel-Based Advanced Porous Silica Materials for Biomedical Applications. *Adv. Funct. Mater.* **2020**, *30*, 1909539.

(21) LaBauve, A. E.; Saada, E. A.; Jones, I. K. A.; Mosesso, R.; Noureddine, A.; Techel, J.; Gomez, A.; Collette, N.; Sherman, M. B.; Serda, R. E.; Butler, K. S.; Brinker, C. J.; Schoeniger, J. S.; Sasaki, D.; Negrete, O. A. Lipid-Coated Mesoporous Silica Nanoparticles for Anti-Viral Applications via Delivery of CRISPR-Cas9 Ribonucleoproteins. *Scientific Reports* **2023**, *13* (1), 1–13.

(22) Butler, K. S.; Durfee, P. N.; Theron, C.; Ashley, C. E.; Carnes, E. C.; Brinker, C. J. Protocells: Modular Mesoporous Silica Nanoparticle-Supported Lipid Bilayers for Drug Delivery. *Small* **2016**, *12*, 2173–2185.

(23) Natarajan, S.; Selvaraj, S. Mesoporous Silica Nanoparticles: Importance of Surface Modifications and Its Role in Drug Delivery. *RSC Adv.* **2014**, *4*, 14328–14334.

(24) Na, H. K.; Kim, M. H.; Park, K.; Ryoo, S. R.; Lee, K. E.; Jeon, H.; Ryoo, R.; Hyeon, C.; Min, D. H. Efficient Functional Delivery of SiRNA Using Mesoporous Silica Nanoparticles with Ultralarge Pores. *Small* **2012**, *8*, 1752–1761.

(25) Xia, T.; Kovochich, M.; Liong, M.; Meng, H.; Kabehie, S.; George, S.; Zink, J. I.; Nel, A. E. Polyethyleneimine Coating Enhances the Cellular Uptake of Mesoporous Silica Nanoparticles and Allows Safe Delivery of SiRNA and DNA Constructs. *ACS Nano* **2009**, *3* (10), 3273–3286.

(26) Li, X.; Chen, Y.; Wang, M.; Ma, Y.; Xia, W.; Gu, H. A Mesoporous Silica Nanoparticle – PEI – Fusogenic Peptide System for SiRNA Delivery in Cancer Therapy. *Biomaterials* **2013**, *34* (4), 1391–1401.

(27) Tsai, P.-H.; Wang, M.-L.; Chang, J.-H.; Yarmishyn, A. A.; Nhi Nguyen, P. N.; Chen, W.; Chien, Y.; Huo, T.-I.; Mou, C.-Y.; Chiou, S.-H. Dual Delivery of HNF4α and Cisplatin by Mesoporous Silica Nanoparticles Inhibits Cancer Pluripotency and Tumorigenicity in Hepatoma-Derived CD133-Expressing Stem Cells. *ACS Appl. Mater. Interfaces* **2019**, *11* (22), 19808–19818.

(28) Wu, M.; Lin, X.; Tan, X.; Li, J.; Wei, Z.; Zhang, D.; Zheng, Y.; Zheng, A.; Zhao, B.; Zeng, Y.; Liu, X.; Liu, J. Photoresponsive Nanovehicle for Two Independent Wavelength Light-Triggered Sequential Release of P-Gp ShRNA and Doxorubicin To Optimize and Enhance Synergistic Therapy of Multidrug-Resistant Cancer. *ACS Appl. Mater. Interfaces* **2018**, *10* (23), 19416–19427.

(29) Yin, P. T.; Pongkulapa, T.; Cho, H.-Y.; Han, J.; Pasquale, N. J.; Rabie, H.; Kim, J.-H.; Choi, J.-W.; Lee, K.-B. Overcoming Chemoresistance in Cancer via Combined MicroRNA Therapeutics with Anticancer Drugs Using Multifunctional Magnetic Core–Shell Nanoparticles. *ACS Appl. Mater. Interfaces* **2018**, *10* (32), 26954–26963.

(30) Zhang, Y.; Sun, C.; Wang, C.; Jankovic, K. E.; Dong, Y. Lipids and Lipid Derivatives for RNA Delivery. *Chem. Rev.* **2021**, *121* (20), 12181–12277.

(31) Kang, J.; Joo, J.; Kwon, E. J.; Skalak, M.; Hussain, S.; She, Z.-G.; Ruoslahti, E.; Bhatia, S. N.; Sailor, M. J. Self-Sealing Porous Silicon-Calcium Silicate Core-Shell Nanoparticles for Targeted SiRNA Delivery to the Injured Brain. *Advanced Materials* **2016**, *36*, 7962.

(32) Faustini, M.; Grosso, D.; Boissière, C. d.; Backov, R.; Sanchez, C. m. "Integrative Sol–Gel Chemistry": A Nanofoundry for Materials Science. *J Sol-Gel Sci Technol*. **2014**, *70*, 216–226.

(33) Durfee, P. N.; Lin, Y.-S.; Dunphy, D. R.; Muniz, A. J.; Butler, K. S.; Humphrey, K. R.; Lokke, A. J.; Agola, J. O.; Chou, S. S.; Chen, I.-M.; Wharton, W.; Townson, J. L.; Willman, C. L.; Brinker, C. J. Mesoporous Silica Nanoparticle-Supported Lipid Bilayers (Protocells) for Active Targeting and Delivery to Individual Leukemia Cells. *ACS Nano* **2016**, *10* (9), 8325–8345.

(34) Noureddine, A.; Hjelvik, E. A.; Croissant, J. G.; Durfee, P. N.; Agola, J. O.; Brinker, C. J. Engineering of Large-Pore Lipid-Coated Mesoporous Silica Nanoparticles for Dual Cargo Delivery to Cancer Cells. *Journal of Sol-Gel Science and Technology* **2019**, *1*, 78.

(35) Mosquera, J.; García, I.; Liz-Marzán, L. M. Cellular Uptake of Nanoparticles versus Small Molecules: A Matter of Size. *Acc. Chem. Res.* **2018**, *51* (9), 2305–2313.

(36) Mindell, J. A. Lysosomal Acidification Mechanisms. *Annual review of physiology* **2012**, *74*, 69–86.

(37) Mintz, P. J.; Kim, J.; Do, K.-A.; Wang, X.; Zinner, R. G.; Cristofanilli, M.; Arap, M. A.; Hong, W. K.; Troncoso, P.; Logothetis, C. J.; Pasqualini, R.; Arap, W. Fingerprinting the Circulating Repertoire of Antibodies from Cancer Patients. *Nature Biotechnology* **2003**, *21* (1), 57.

(38) Arap, M. A.; Lahdenranta, J.; Mintz, P. J.; Hajitou, A.; Sarkis, Á. S.; Arap, W.; Pasqualini, R. Cell Surface Expression of the Stress Response Chaperone GRP78 Enables Tumor Targeting by Circulating Ligands. *Cancer Cell* **2004**, *6* (3), 275–284.

(39) Butler, K. S.; Brinker, C. J.; Leong, H. S. Bridging the In Vitro to In Vivo Gap: Using the Chick Embryo Model to Accelerate Nanoparticle Validation and Qualification for In Vivo Studies. *ACS Nano* **2022**, *16* (12), 19626–19650.

(40) Paul Garcia; Yan Wang; Jean Viallet; Zuzana Macek Jilkova. The Chicken Embryo Model: A Novel and Relevant Model for Immune-Based Studies. *Front. immunol.* **2021**, *12,* 791081.

(41) Croissant, J. G.; Fatieiev, Y.; Khashab, N. M. Degradability and Clearance of Silicon, Organosilica, Silsesquioxane, Silica Mixed Oxide, and Mesoporous Silica Nanoparticles. *Advanced Materials* **2017**, *29* (9).